



# Multi-Objective Optimization of Process Parameters in Laser Cladding CoCrCuFeNi High-Entropy Alloy Coating

Yubin Huang<sup>1</sup> · Yongle Hu<sup>1,2</sup> · Mingjun Zhang<sup>1</sup> · Cong Mao<sup>1</sup> · Kaiming Wang<sup>1,3</sup> ·  
Yonggang Tong<sup>1</sup> · Jian Zhang<sup>1</sup> · Kangwei Li<sup>1</sup>

Submitted: 8 January 2022 / in revised form: 24 March 2022 / Accepted: 14 April 2022 / Published online: 6 May 2022  
© ASM International 2022

**Abstract** Laser cladding of CoCrCuFeNi high-entropy alloy (HEA) coatings onto 45 steel was successfully performed using a 3-kW fiber laser. The effect of process parameters (laser power, scanning speed and powder feeding rate) on responses (aspect ratio, dilution rate and microhardness) was systematically investigated based on response surface methodology (RSM). Process optimization was carried out to acquire the desired coating with a maximum aspect ratio and microhardness and a dilution rate of 10~20%. A laser power of 773.65 W, scanning speed of 5 mm/s and powder feeding rate of 15 g/min were found to be the optimum parameters. The aspect ratio, dilution rate and microhardness of the optimized CoCrCuFeNi coating were determined to be 5.07, 14.29% and 186.8 HV, respectively. Validation experiments under optimum conditions reveal that the predicted values agree well with the actual values within a relative error of 10%. Finally, the microstructure and the microhardness distribution were characterized. The XRD results, together with

the mixing entropy value, confirm that the optimized CoCrCuFeNi coating belongs to HEAs.

**Keywords** CoCrCuFeNi high-entropy alloy (HEA) coating · laser cladding · process optimization · response surface methodology (RSM)

## Introduction

High-entropy alloys (HEAs) are a new type of alloy containing multiple elements, where the content of each element ranges between 5 and 35 at.% (Ref 1). HEAs are inclined to form single-phase solid solutions and nanosized precipitates rather than brittle phases or other intermetallic compounds, which is primarily attributed to the high-entropy effect and the sluggish diffusion effect in HEAs (Ref 2). Therefore, HEAs usually possess excellent properties in terms of high strength (Ref 3, 4), excellent wear performance (Ref 5, 6), thermal stability (Ref 7, 8), oxidation resistance (Ref 9, 10) and favorable corrosion resistance (Ref 11, 12). Owing to these characteristics, HEAs have attracted widespread attention in scientific research and engineering applications (Ref 13).

To date, many methods, such as laser cladding (LC), plasma cladding, thermal spraying, magnetron sputtering and mechanical alloying, have been adopted to fabricate different HEA coatings (Ref 14). Among them, LC emits less pollution, has a high work efficiency and can be applied to fabricate thick coatings, all of which offer advantages over other surface treatment processes (Ref 15). In addition, the rapid cooling rate during LC can improve the microstructure and stabilize the phase (Ref 16). Moreover, laser-clad HEA coatings generally exhibit a small dilution rate and excellent metallurgical bonding

✉ Yubin Huang  
huangyb@stu.csust.edu.cn

Mingjun Zhang  
mj\_zhang@csust.edu.cn

<sup>1</sup> Hunan Provincial Key Laboratory of Intelligent Manufacturing Technology for High-performance Mechanical Equipment, Changsha University of Science and Technology, Changsha 410114, People's Republic of China

<sup>2</sup> Hunan Engineering Research Center for Heat Treatment Technology and Equipment, Zhuzhou 412007, People's Republic of China

<sup>3</sup> State Key Laboratory of Tribology, Department of Mechanical Engineering, Tsinghua University, Beijing 100084, People's Republic of China

with the substrate, which is beneficial for engineering applications (Ref 17).

As often reported (Ref 13, 18), the LC process parameters, especially laser power, scanning speed and powder feeding rate, provide a significant effect on the geometries and properties of HEA coatings. Chao et al. (Ref 19) fabricated  $Al_xCoCrFeNi$  HEA coatings and found that an increase in laser power produced coatings with larger depths and widths. Conversely, these two geometrical features exhibited a decrease in dimension with increasing laser beam size and scanning speed, while the powder feeding rate had a negligible influence on these features. Shu et al. (Ref 20) synthesized a  $CoCrBFeNiSi$  HEA amorphous coating and found that an increase in laser power reduced the amorphous phase content inside the coating, which subsequently results in a lower microhardness and worse wear resistance. Zhang et al. (Ref 21) investigated the relationship between LC process parameters and properties for fabricating  $FeNiCoCrTi_{0.5}$  HEA coating. The results showed that an increase in specific energy (defined as laser power divided by the production of scanning speed and spot diameter) increased the dilution rate, consequently leading to a decrease in the microhardness of the coating. Ni et al. (Ref 22) investigated the influence of scanning speed on an  $Al_{0.5}FeCu_{0.7}NiCoCr$  HEA coating and successfully developed a defect-free coating with superior microhardness at the highest scanning speed due to the ultrafine microstructure generated inside the coating. Yue et al. (Ref 23) synthesized a laser-clad  $AlFeCoCrNiCu$  HEA coating on a magnesium substrate. As a result, a large amount of Mg was observed in the lower part of the coating due to severe dilution, which can degrade the properties of the coating.

Clearly, the laser process parameters that affect the geometry and property of the HEA coatings usually depend upon the combination of two or more parameters. Therefore, it is recommended to reduce experimental efforts and achieve the optimal value for each parameter through the design of experiments (DOE) (Ref 24). For instance, Ma et al. (Ref 25) investigated the influence of process parameters (laser power, scanning speed and defocus amount) on responses (dilution rate and residual stress) while preparing a  $CoCr_{1.5}FeNiNb_{0.5}$  HEA coating. The empirical models between parameters and responses were established using analysis of variance (ANOVA) and response surface methodology (RSM). The minimum dilution and residual stress were obtained via multi-objective quantum-behaved particle swarm optimization. Similarly, Dada et al. (Ref 26) optimized the process parameters (laser power and scanning speed) to obtain the maximum microhardness of HEA coatings via RSM. The established microhardness model revealed a strong correlation between the predicted response and the actual value.

Siddiqui et al. (Ref 27) prepared an  $AlCu_{0.5}FeNiTi$  HEA coating on an aluminum substrate. The effect of laser power, scanning speed and powder feeding rate on aspect ratio, dilution rate and clad angle was investigated using ANOVA and regression analysis (RA) techniques. The experimental results indicated an evident reduction in defects and enhancement in geometrical features of the HEA coating with optimum parameters.

In the previous literature related to LC HEA coatings, the effects of process parameters on geometry and microhardness have not been studied simultaneously. However, the geometry and microhardness are interrelated. For example, the correlation between dilution rate and microhardness can be positive (Ref 28) or negative (Ref 29). It is, therefore, necessary to take into account the geometry and microhardness of the HEA coating when investigating the effects of the LC process parameters. The Co-Cr-Cu-Fe-Ni HEA system is a well-known and frequently used HEA system (Ref 7, 30). For LC HEA coatings, the multi-objective optimization of process parameters and their synergic effect on geometry and microhardness is rare in the literature, especially in regard to  $CoCrCuFeNi$  HEA coatings. Therefore, based on the RSM technique, this paper carried out a study of laser cladding  $CoCrCuFeNi$  HEA coatings on 45 steel to investigate the effects of process parameters (laser power, scanning speed and powder feeding rate) on the output responses (aspect ratio, dilution rate and microhardness) and to optimize the process parameters for acquiring the desired coating with maximum aspect ratio and microhardness and a dilution rate of 10~20%. Finally, microstructure analysis, as well as XRD and EDS tests, was conducted for the optimized HEA coating.

## Experimental Setup

### Materials and Equipment

Commercial Co, Cr, Cu, Fe and Ni powders (Changsha Tianjiu Metal Materials Co., LTD) with 99.99% purity and size range of  $-150+300$  mesh were selected as the cladding material. These pure powders were weighed according to the nominal composition of  $CoCrCuFeNi$  (1:1:1:1:1 in molar ratio) and then mixed for two hours via ball milling with a speed of 300 rpm and a ball-to-powder ratio of 2:1 (mass ratio). Normalized 45 steel (100 mm  $\times$  100 mm  $\times$  10 mm) was selected as the cladding substrate after being ground with sandpaper and cleaned with ethanol.

The equipment setup is shown in Fig. 1. The LC experiments were performed using a 3-kW fiber laser (YLS-3000, IPG Photonics Co., Germany) at a wavelength

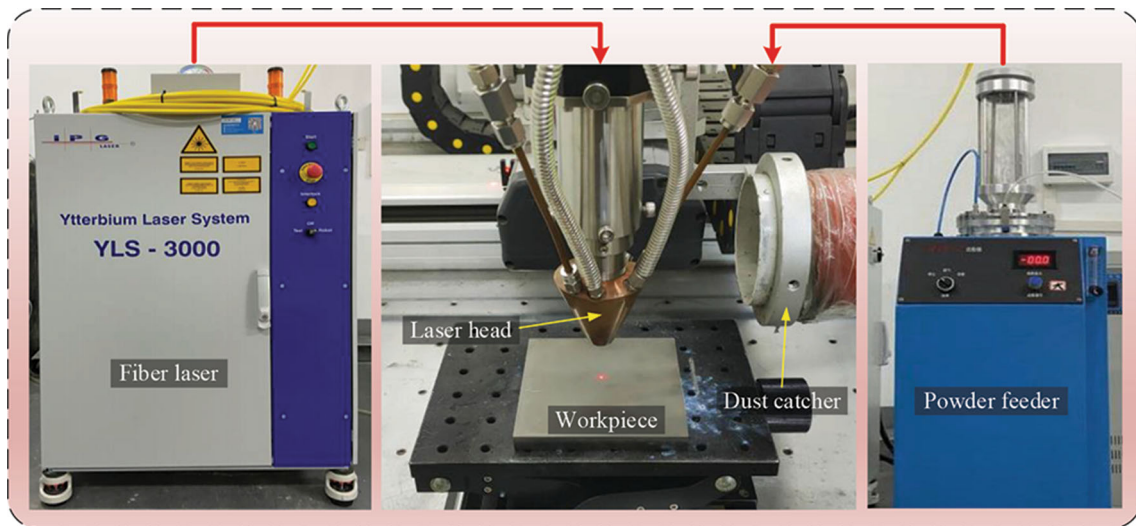


**Fig. 1** Equipment setup

of 1070 nm and a spot diameter of 1.8 mm. The defocus was set to 20 mm, and argon gas was applied as the shielding gas with a flow rate of 10 L/min.

The clad specimens were cut perpendicular to the laser scanning direction to obtain the cross-section morphology. The cross sections of the cut specimens were ground by 400-3000 mesh sandpapers, polished with a polishing agent and then etched using CuSO<sub>4</sub>/H<sub>2</sub>SO<sub>4</sub>/HCl=5:5:100 (volume ratio). The geometrical features (width *W*, height *H* and depth *h*) and microstructures of the coatings were observed using a stereomicroscope (Leica S9i, Germany) and scanning electron microscope (SEM, ProX, Netherlands) equipped with energy dispersive spectroscopy (EDS), respectively. A semiautomatic Vickers hardness tester (HVST-1000Z) was applied for microhardness measurement with a load of 100 g and a duration time of 10 s. The microhardness of each coating was calculated from the average hardness value of three test points close to the coating surface (cross section). An x-ray diffractometer with a Cu K $\alpha$  source (XRD, D/MAX-Rapid X, Japan) was used to analyze the phase component of the coatings.

**Method of Analysis**

The RSM is a mathematical approach used to establish reliable empirical relationships between input variables and output responses (Ref 31). The second-order response surface model for the three factors is given by Eq. 1:

$$y = \beta_0 + \sum_{i=1}^3 \beta_i x_i + \sum_{i=1}^3 \beta_{ii} x_i^2 + \sum_{i=1}^3 \sum_{j=1}^3 \beta_{ij} x_i x_j + \varepsilon \quad (\text{Eq 1})$$

where *x* and *y* are the independent variables and predicted response, respectively;  $\beta_0$  demonstrates the coefficient of

**Table 1** Input factors with designed levels

Factors	Notation (units)	Levels		
		-1	0	1
Laser power	<i>P</i> (W)	600	850	1100
Scanning speed	<i>V</i> (mm/s)	2	3.5	5
Powder feeding rate	<i>F</i> (g/min)	15	16.5	18

the constant term;  $\beta_i$ ,  $\beta_{ii}$ , and  $\beta_{ij}$  are the coefficients of the linear, quadratic and interaction effects, respectively; and  $\varepsilon$  denotes the statistical error.

The DOE was performed using Design-Expert 13 software (Stat-Ease Inc., USA) with Box–Behnken design (BBD). The BBD is a widely used experimental technique for optimization, as it can reduce experimental costs compared with full-factorial experiments. According to the preliminary test results, the range of each process parameter shown in Table 1 was determined on the premise that the coatings can be continuous without apparent defects on the surface. The level of each process parameter was divided into three levels in BBD, namely -1 (lower), 0 (center point) and 1 (higher). The output responses included the aspect ratio, dilution rate and microhardness of the laser-clad coatings. A schematic diagram of a typical laser-clad coating is shown in Fig. 2. The expressions for the aspect ratio and dilution rate are defined by Eqs. 2 and 3, respectively. The BBD matrix and output responses are listed in Table 2. Figure 3 presents the cross section of seventeen single-track LC coatings corresponding to Table 2.

$$\text{Aspect ratio}(W/H) = \frac{W}{H} \tag{Eq 2}$$

$$\text{Dilution rate } (\eta) = \frac{h}{H + h} \times 100\% \tag{Eq 3}$$

## Results and Discussion

### Effect of Process Parameters on Aspect Ratio

The results obtained from the ANOVA for the aspect ratio are given in Table 3. The F-value is used to evaluate the influence of factors on the response. The higher the F-value, the greater the influence of this factor on the response. In this case, the scanning speed, with an F-value

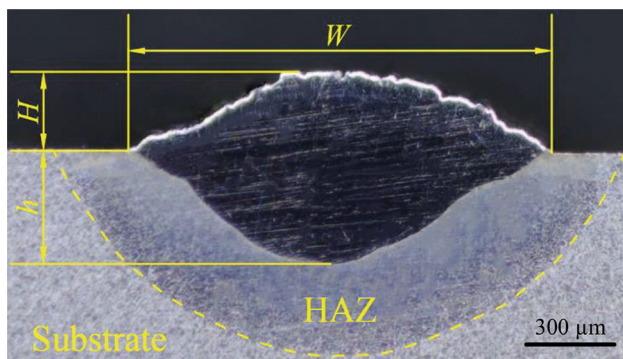


Fig. 2 Schematic diagram of a laser-clad coating

of 6.7400, has the largest effect on the aspect ratio, followed by the laser power and powder feeding rate. Any factor with a P-value less than 0.05 was considered significant (Ref 31). Thus, the aspect ratio model with a P-value of 0.0355 is of great significance. Only the interaction between scanning speed and powder feeding rate ( $VF$ ) was found to be significant among all the interaction terms. The laser power ( $P^2$ ) and the powder feeding rate ( $F^2$ ) are both significant quadratic terms with regard to the aspect ratio. An insignificant lack of fit (P-value > 0.05) means that the model fits the data within the observed variation.  $R^2$  measures the amount of variation around the mean explained by the model. For a well-fitted model,  $R^2$  should be greater than 0.8 (Ref 32). An  $R^2$  value of 0.8442 implies that 84.42% of the experimental data can be explained by this model. Adequate precision measures the signal-to-noise ratio, and a ratio of 8.4998 (>4) reveals adequate precision for the established model (Ref 33). After removing insignificant terms, the regression equations used to predict the aspect ratio with coded and actual factors are given in Eqs. 4 and 5, respectively:

$$\begin{aligned} W/H_{\text{coded}} = & 3.64 + 0.6163V - 1.05VF - 0.945P^2 \\ & + 0.8525F^2 \end{aligned} \tag{Eq 4}$$

$$\begin{aligned} W/H_{\text{actual}} = & 67.82474 + 8.30739V - 0.467778VF \\ & - 0.000015P^2 + 0.378889F^2 \end{aligned} \tag{Eq 5}$$

The accuracy of the aspect ratio model can be further verified by the diagnostic plots (Fig. 4), which include the

Table 2 BBD matrix and output responses

No.	Factors			Responses		
	$P, W$	$V, \text{ mm/s}$	$F, \text{ g/min}$	$W/H$	Dilution rate, %	Microhardness, HV
1	850	2	18	4.60	50.64	168.62
2	1100	3.5	18	3.45	55.84	159.62
3	850	2	15	2.05	50.88	168.54
4	850	3.5	16.5	4.72	59.60	172.64
5	850	3.5	16.5	3.20	47.57	170.71
6	600	5	16.5	1.73	5.02	184.72
7	850	3.5	16.5	3.50	50.06	170.56
8	1100	2	16.5	2.37	62.98	155.13
9	850	5	18	4.22	13.58	177.44
10	850	5	15	5.88	14.06	174.82
11	600	2	16.5	1.67	17.53	178.02
12	1100	5	16.5	3.79	52.52	166.56
13	600	3.5	18	2.75	10.38	179.65
14	850	3.5	16.5	3.53	49.92	171.52
15	850	3.5	16.5	3.25	48.56	168.73
16	1100	3.5	15	4.35	62.60	158.62
17	600	3.5	15	3.64	12.48	179.47

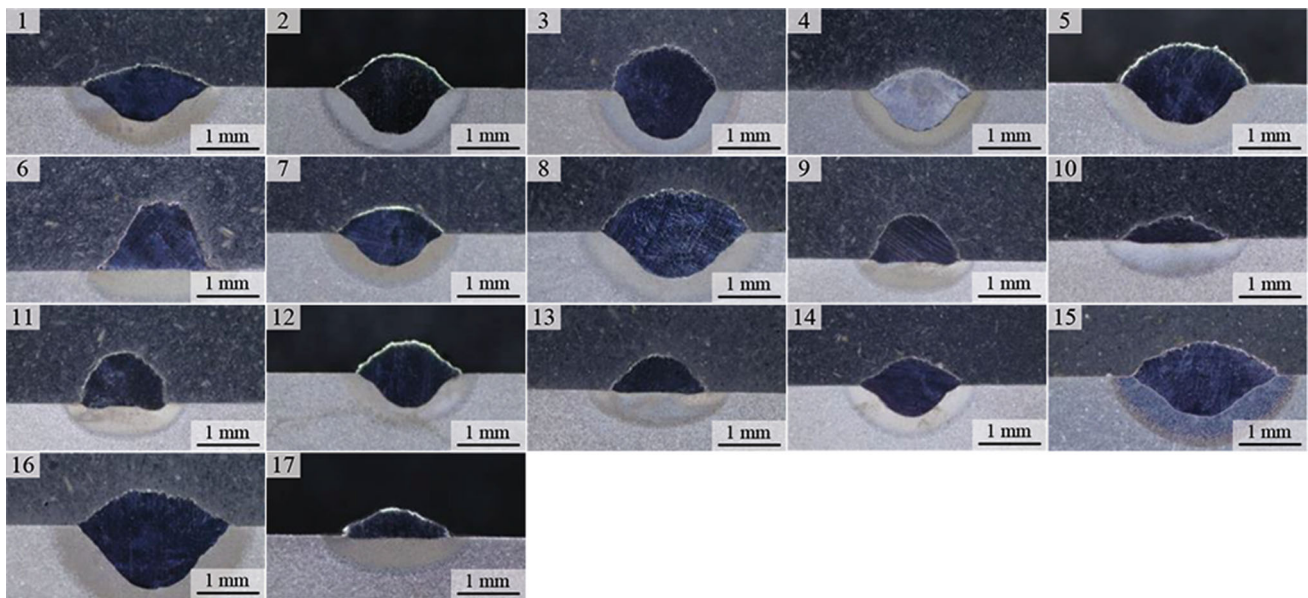


**Fig. 3** Cross section of seventeen single-track LC coatings corresponding to Table 2

**Table 3** ANOVA for aspect ratio

Source	Sum of squares	df	Mean squares	F-value	P-value	
Model	17.0900	9	1.9000	4.2100	0.0355	Significant
<i>P</i>	2.1700	1	2.1700	4.8200	0.0641	
<i>V</i>	3.0400	1	3.0400	6.7400	0.0356	
<i>F</i>	0.1013	1	0.1013	0.2247	0.6499	
<i>PV</i>	0.4624	1	0.4624	1.0300	0.3448	
<i>PF</i>	0.0000	1	0.0000	0.0001	0.9943	
<i>VF</i>	4.4300	1	4.4300	9.8300	0.0165	
<i>P</i> <sup>2</sup>	3.7600	1	3.7600	8.3400	0.0234	
<i>V</i> <sup>2</sup>	0.3917	1	0.3917	0.8692	0.3822	
<i>F</i> <sup>2</sup>	3.0600	1	3.0600	6.7900	0.0351	
Residual	3.1500	7	0.4506			
Lack of fit	1.6100	3	0.5369	1.3900	0.3673	Not significant
Pure error	1.5400	4	0.3859			
Cor total	20.2500	16				
<i>R</i> <sup>2</sup>	0.8442		Adeq precision	8.4998		

normal plot of residuals (Fig. 4a) and the predicted vs. actual plot (Fig. 4b). The points in Fig. 4(a) lie close to a straight line, revealing that the residuals are approximately normally distributed. It is demonstrated that the predicted values agree well with the actual values (Fig. 4b); thus, the model for the aspect ratio can be used as a constraint function.

The perturbation plot shown in Fig. 5(a) describes the effect of process parameters on aspect ratio, where A, B and C, respectively, symbolize laser power, scanning speed

and powder feeding rate. It is explicitly observed that the variation range for the scanning speed is more conspicuous than that for laser power and powder feeding rate, well-proven by the largest F-value and the smallest P-value for the scanning speed given in Table 3. Specifically, the scanning speed has a positive effect on the aspect ratio. As the scanning speed increases, the metal powder does not have enough time to accumulate in the vertical direction; thus, the layer height manifests a downward trend, leading to a larger aspect ratio. Before the center point, the laser

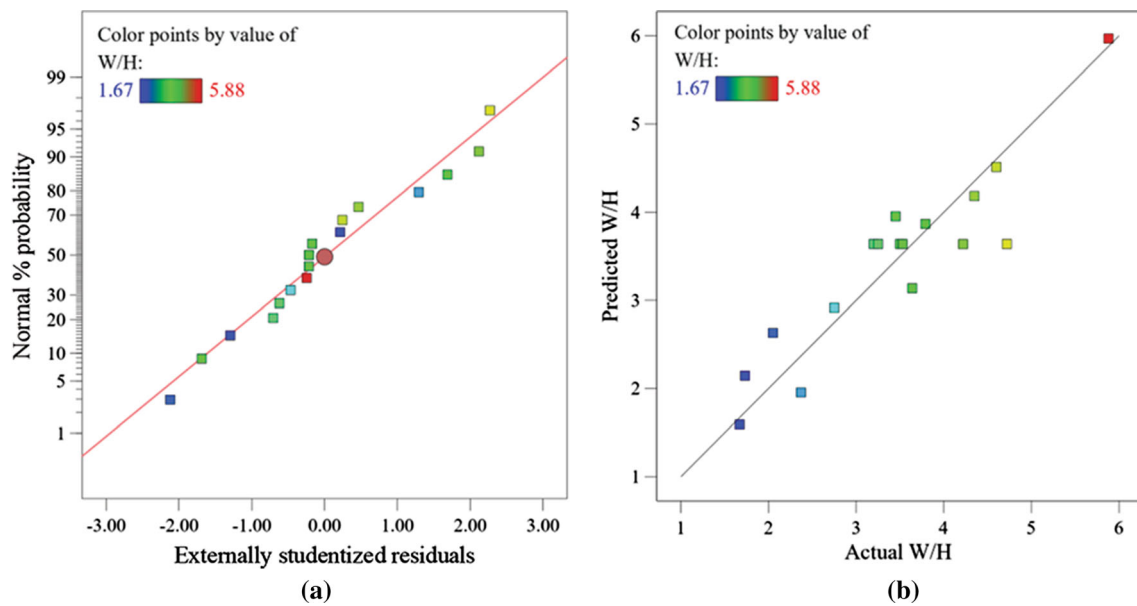


**Fig. 4** Diagnostic plots for aspect ratio: (a) normal plot of residuals and (b) predicted vs. actual plot

power has a positive effect on the aspect ratio since an increase in the laser power produces a deeper molten pool, making it difficult for the cladding layer to accumulate vertically. As the powder feeding rate increases, the height of the powder layer deposited on the substrate increases, and more heat is used to melt the metal powder instead of the substrate, forming a narrow and thick coating; thus, the aspect ratio presents a decreasing trend. After the center point, the amount of powder melting per unit time increases with laser power, while the increase in layer height is more obvious than that of layer width (Ref 34), leading to a decrease in the aspect ratio. With a continuous increase in the powder feeding rate, the liquid metal spreads along the width direction as a result of gravity and surface tension, which increases the aspect ratio of the coating.

The contour plots given in Figs. 5(b)–(d) demonstrate the interaction between laser power and scanning speed, laser power and powder feeding rate, scanning speed and powder feeding rate on aspect ratio, respectively. As shown in Fig. 5(b), the aspect ratio increases with the laser power and scanning speed. When the scanning speed is kept at a low level, laser powers that are both too high and too low are not conducive to increasing the aspect ratio. Increasing the laser power results in a larger aspect ratio over the whole range of powder feeding rates, as shown in Fig. 5(c). Furthermore, a larger aspect ratio can be obtained with a higher or lower powder feeding rate when the level of the laser power is low. Figure 5(d) illustrates that the closer the reference point is to the center of the design space, the smaller the aspect ratio becomes. That is, when the coded units of scanning speed and powder feeding rate are both at

approximately the zero level, the aspect ratio reaches its lowest value.

#### Effect of process parameters on dilution rate

The ANOVA for dilution rate is given in Table 4. The F-value of the model is 12.1800, and the P-value is less than 0.05, indicating that the model is significant. With an F-value of 72.8800, the laser power has the greatest influence on the dilution rate. The scanning speed and powder feeding rate have less influence on the dilution rate than the laser power. The scanning speed ( $V^2$ ) and powder feeding rate ( $F^2$ ) are both significant quadratic terms. The lack of fit P-value is 0.0834, which means that the model is desirable. An  $R^2$  value of 0.9400 indicates that the dilution rate model reasonably describes the relationship between process parameters and output responses. The adequate precision (signal-to-noise ratio) is greater than 4, implying that this model can be applied to navigate the design space. Considering the significant model terms, Eqs. 6 and 7 represent the regression equations for the dilution rate based on coded and actual values, respectively.

$$\eta_{\text{coded}} = 51.14 + 23.57P - 12.11V - 9.83V^2 - 9.02F^2 \quad (\text{Eq 6})$$

$$\eta_{\text{actual}} = -1252.10510 + 0.325627P + 21.79672V - 4.36989V^2 - 4.00878F^2 \quad (\text{Eq 7})$$

Figure 6(a) presents the normal probability plots for the residuals that fall in a straight line, implying a normal distribution for the residuals. It can be inferred from

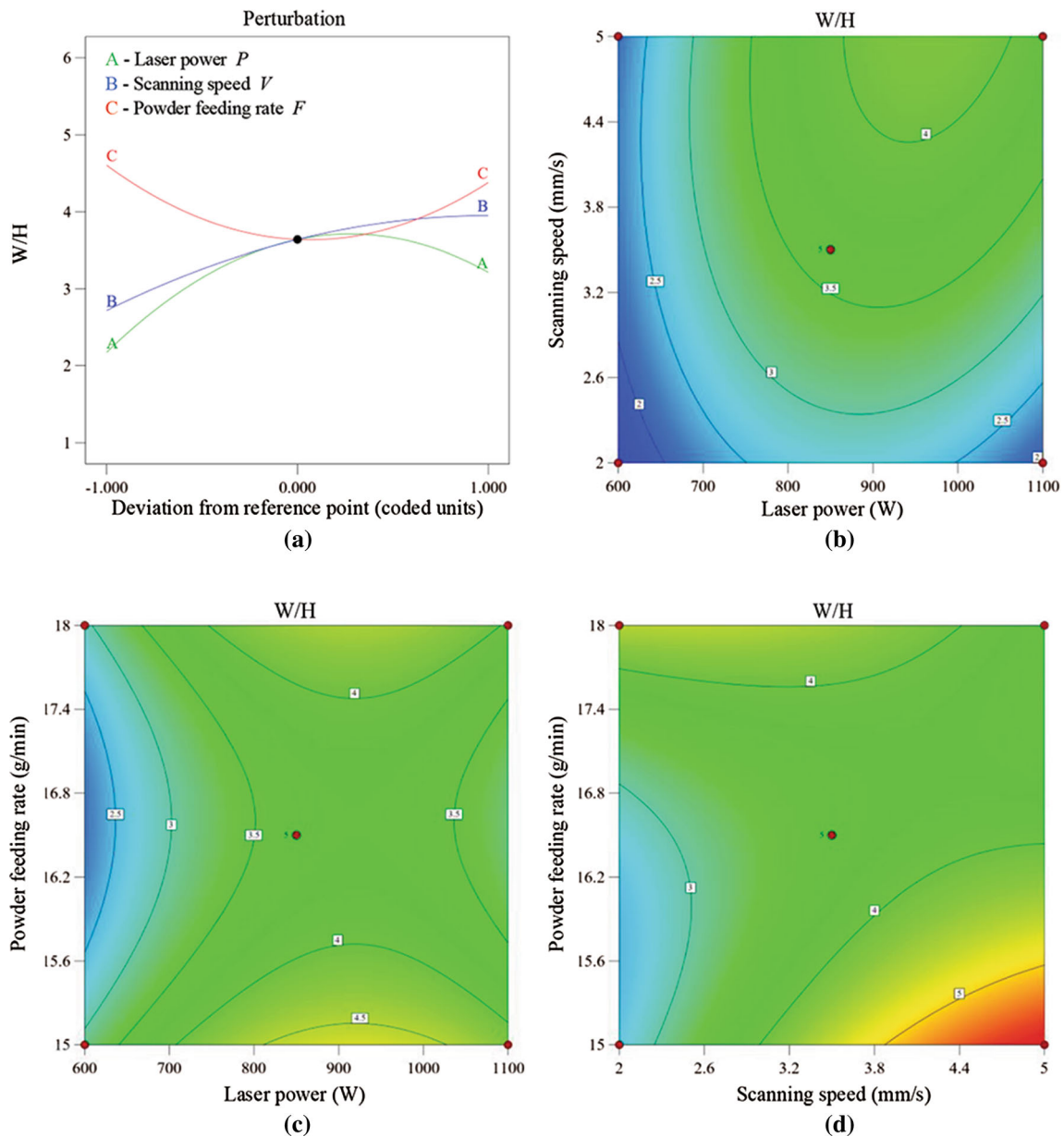


**Fig. 5** Effect of process parameters on aspect ratio: (a) perturbation plot; (b)  $P$  and  $V$ ; (c)  $P$  and  $F$  and (d)  $V$  and  $F$

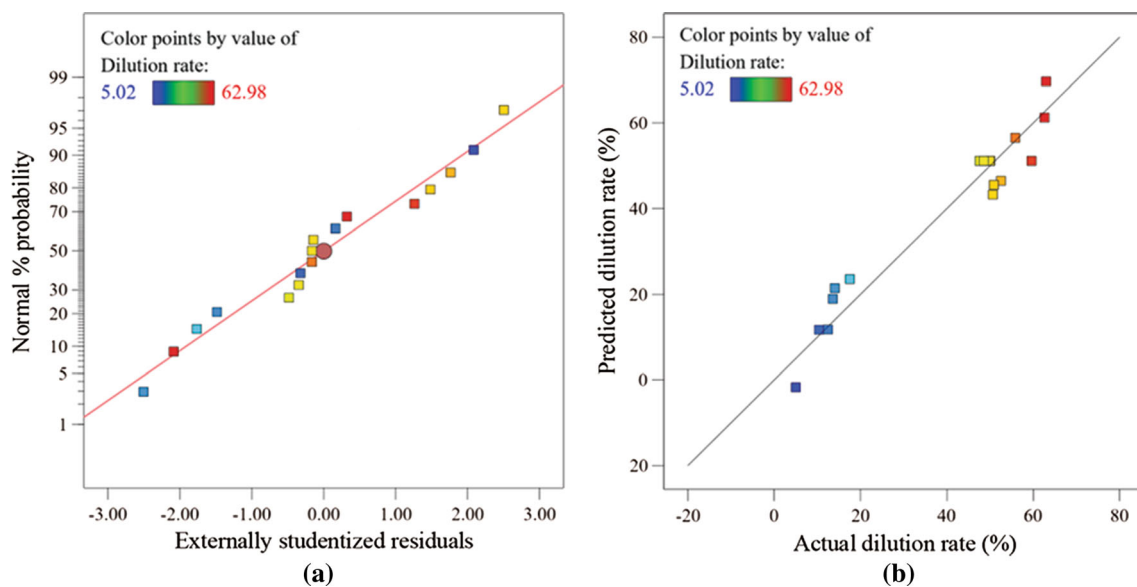
Fig. 6(b) that the predicted results are in agreement with those obtained from the experiment. Therefore, the model for dilution rate reveals a high degree of accuracy.

It is evident from the perturbation plot (Fig. 7a) that the laser power has the greatest effect on the dilution rate, followed by scanning speed and powder feeding rate, which agrees well with the analysis results given in Table 4. Figure 7(a) shows that the laser power has a negative effect on reducing the dilution rate. Specifically, an increase in laser power generates a deeper molten pool,

thereby increasing the dilution rate. A reduction in dilution rate occurs with increasing scanning speed. Although the powder injected into the molten pool per unit area decreases with increasing scanning speed, the heat input also decreases correspondingly, resulting in a reduced dilution rate. With an increase in the powder feeding rate, the dilution rate displays a downward trend, which can be ascribed to the shading effect of the metal powder. The attenuation rate of the laser energy is approximately proportional to the powder feeding rate (Ref 35). The larger

**Table 4** ANOVA for dilution rate

Source	Sum of squares	df	Mean squares	F-value	P-value	
Model	6685.1200	9	742.7900	12.1800	0.0017	Significant
<i>P</i>	4442.9500	1	4442.9500	72.8800	<0.0001	
<i>V</i>	1172.9500	1	1172.4900	19.2300	0.0032	
<i>F</i>	11.4700	1	11.4700	0.1882	0.6775	
<i>PV</i>	1.0500	1	1.0500	0.0172	0.8993	
<i>PF</i>	5.4300	1	5.4300	0.0890	0.7741	
<i>VF</i>	0.0144	1	0.0144	0.0002	0.9882	
<i>P</i> <sup>2</sup>	194.5400	1	194.5400	3.1900	0.1172	
<i>V</i> <sup>2</sup>	407.0400	1	407.0400	6.6800	0.0363	
<i>F</i> <sup>2</sup>	342.5500	1	342.5500	5.6200	0.0496	
Residual	426.7500	7	60.9600			
Lack of fit	333.1300	3	111.0400	4.7400	0.0834	Not significant
Pure error	93.6300	4	23.4100			
Cor total	7111.8800	16				
R <sup>2</sup>	0.9400			Adeq precision	11.9138	

**Fig. 6** Diagnostic plots for dilution rate: (a) normal plot of residuals and (b) predicted vs. actual plot

the powder feeding rate, the greater the attenuation of laser energy, resulting in reduced melting of the substrate and dilution rate.

The contour plots shown in Fig. 7(b)–(d) illustrate the interaction between laser power and scanning speed, laser power and powder feeding rate, scanning speed and powder feeding rate on dilution rate, respectively. Figure 7(b) shows that reducing the laser power or increasing the scanning speed (less heat input) is beneficial for a low dilution rate. It is evident in Fig. 7(c) that the dilution rate increases with increasing laser power over the whole range of powder feeding rates. In addition, if the laser power is kept constant, the dilution rate decreases at a higher or lower powder feeding rate. A low dilution rate can be

obtained at a high scanning speed if the powder feeding rate remains unchanged, as shown in Fig. 7(d).

### Effect of Process Parameters on Microhardness

Table 5 demonstrates the ANOVA for microhardness. The F-value of the model is 80.6500, which means that the statistical model is significant for microhardness, and there is only a 0.01% probability that an F-value this large can occur due to noise. A P-value lower than 0.05 indicates that the model term is significant. In this case, the laser power, scanning speed, quadratic order of laser power ( $P^2$ ) and scanning speed ( $V^2$ ) are all significant model terms. The lack of fit is not significant, which means that the model is



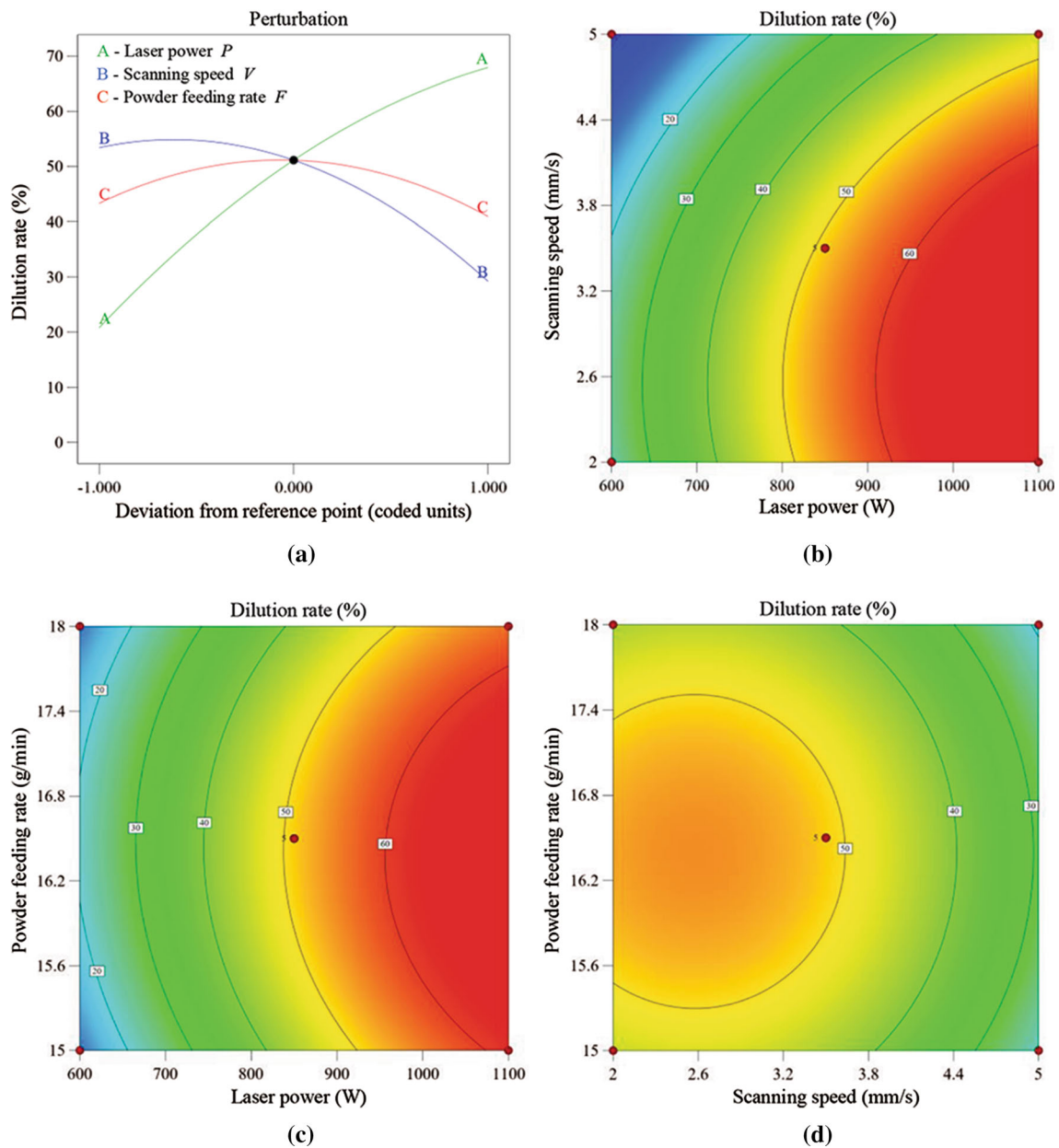


**Fig. 7** Effect of process parameters on dilution rate: (a) perturbation plot; (b)  $P$  and  $V$ ; (c)  $P$  and  $F$  and (d)  $V$  and  $F$

desirable. The value of  $R^2$  is extremely close to 1, indicating that the mathematical model agrees well with the experimental data. The adequate precision is 31.9054, which reveals a high accuracy for the established model. After eliminating the insignificant terms, the regression equations for microhardness in terms of coded and actual values are represented in Eqs. 8 and 9, respectively:

$$\text{Microhardness}_{\text{coded}} = 170.83 - 10.24P + 4.15V - 1.37P^2 + 1.65V^2 \tag{Eq 8}$$

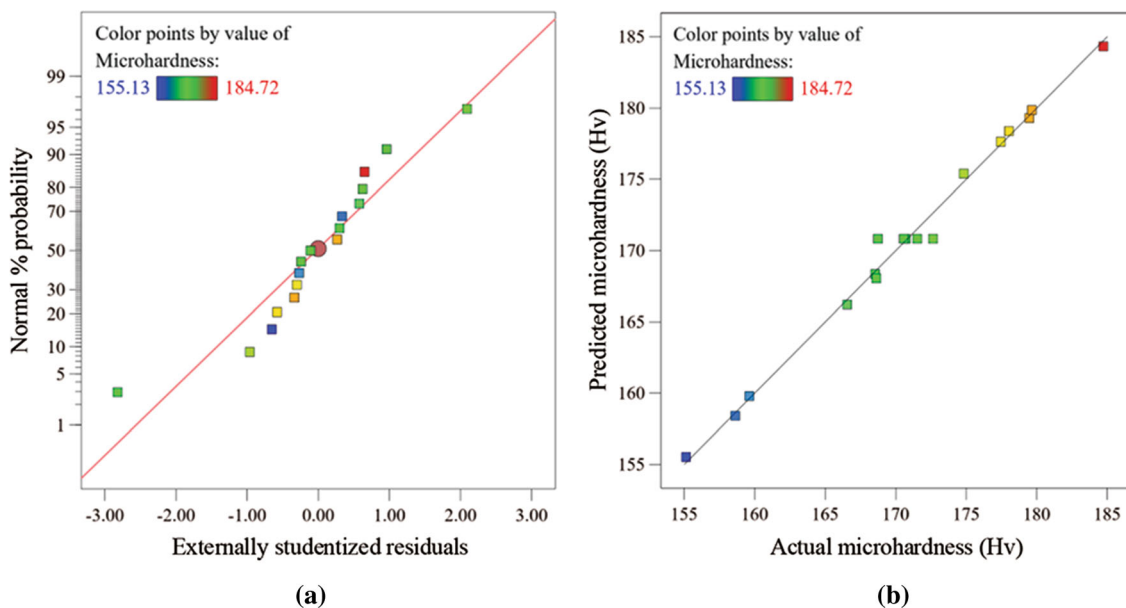
$$\begin{aligned} \text{Microhardness}_{\text{actual}} = & 202.30258 - 0.023764P \\ & - 9.68639V - 0.000022P^2 \\ & + 0.731222V^2 \end{aligned} \tag{Eq 9}$$

It can be inferred from Fig. 8(a) that the residual values of the microhardness model are generally distributed in a straight line. Figure 8(b) further confirms the model, as there is a strong correlation between the predicted and actual values.

Figure 9(a) presents a perturbation plot to illustrate the effects of process parameters on microhardness at the center point in the design space. The microhardness of the

**Table 5** ANOVA for microhardness

Source	Sum of squares	df	Mean squares	F-value	P-value	
Model	1004.7500	9	111.6400	80.6500	<0.0001	Significant
<i>P</i>	839.0700	1	839.0700	606.1700	<0.0001	
<i>V</i>	138.0300	1	138.0300	99.7200	<0.0001	
<i>F</i>	1.8800	1	1.8800	1.3600	0.2818	
<i>PV</i>	5.5900	1	5.5900	4.0400	0.0843	
<i>PF</i>	0.1681	1	0.1681	0.1214	0.7377	
<i>VF</i>	1.6100	1	1.6100	1.1700	0.3162	
<i>P</i> <sup>2</sup>	7.9000	1	7.9000	5.7100	0.0482	
<i>V</i> <sup>2</sup>	11.4000	1	11.4000	8.2300	0.0240	
<i>F</i> <sup>2</sup>	0.0629	1	0.0629	0.0455	0.8372	
Residual	9.6900	7	1.3800			
Lack of fit	1.4400	3	0.4800	0.2327	0.8695	Not significant
Pure error	8.2500	4	2.0600			
Cor total	1014.4400	16				
<i>R</i> <sup>2</sup>	0.9904		Adeq precision	31.9054		

**Fig. 8** Diagnostic plots for microhardness: (a) normal plot of residuals and (b) predicted vs. actual plot

coating decreases with increasing laser power. This is because an increase in laser power leads to increased melting of the substrate; thus, the dilution rate increases. (The effect of the dilution rate on microhardness is discussed later.) Additionally, a larger heat input results in coarse microstructures in the coating. According to Hall–Petch theory, a coarse microstructure is not conducive to improving the microhardness (Ref 36). Increasing the scanning speed plays a positive role in improving the microhardness, as an increase in scanning speed leads to less heat input on the substrate. On the one hand, less heat input reduces the dilution rate. On the other hand, due to the accelerated cooling rate of the molten pool, a larger

undercooling increases the nucleation rate, which leads to refinement of the microstructure and improvement of microhardness (Ref 37). In contrast, the powder feeding rate has little effect on microhardness, which is also proven by its small F-value and insignificant P-value, as given in Table 5. Since the microhardness remains almost unchanged under different powder feeding rates, the interaction for *P/F* and *V/F* is not discussed in this research.

The effect of the interaction between laser power and scanning speed on microhardness is shown in Fig. 9(b). Notably, the microhardness increases with decreasing laser power and increasing scanning speed. A combination of Fig. 7(b) and 9(b) shows that there is an inverse

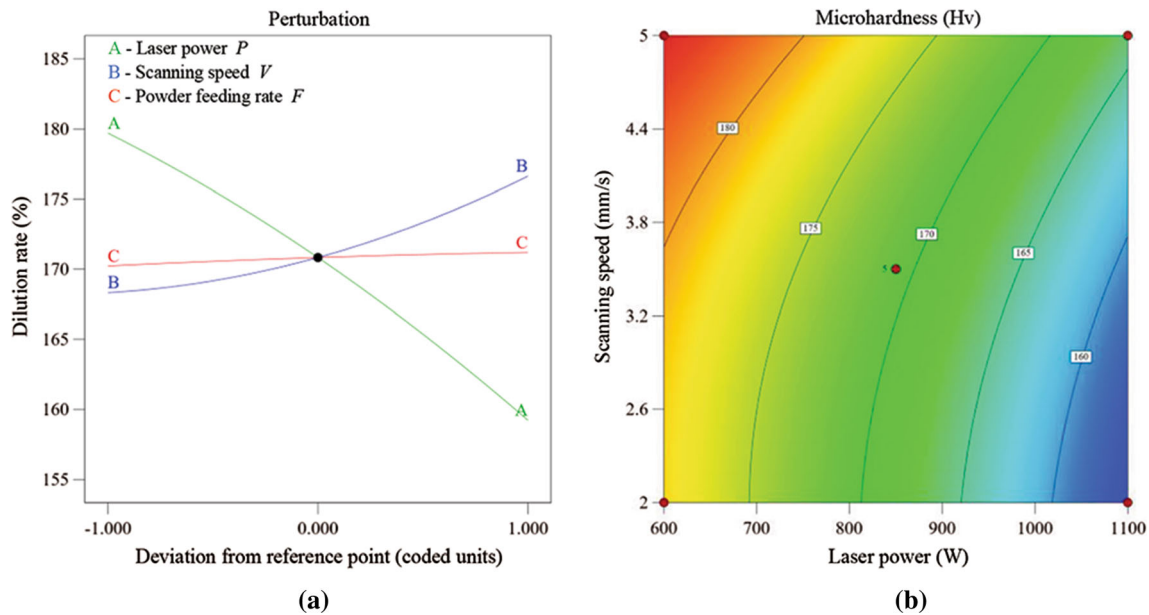


Fig. 9 Effect of process parameters on microhardness: (a) perturbation plot and (b)  $P$  and  $V$

relationship between microhardness and dilution rate, that is, the microhardness of the coating decreases as the dilution rate increases. This is because the substrate mainly contains the Fe element, and an increase in dilution rate results in a more Fe element being mixed into the CoCrCuFeNi coating. On the one hand, a higher Fe content leads to a decrease in the unstable stacking fault energy ( $\gamma_{USFE}$ ) of the coating, resulting in a decrease in the Hall–Petch coefficient (Ref 38). The Hall–Petch coefficient can be used to evaluate grain boundary strengthening (Ref 39, 40), and the smaller the Hall–Petch coefficient, the weaker the effect of grain boundary strengthening. Similar results have been obtained in other studies (Ref 41, 42). On the other hand, the relative proportion of Cr content in the coating decreases with increasing Fe content. Compared with other elements in the CoCrCuFeNi coating, the effect of Cr on solid solution strengthening is more pronounced (Ref 43). Therefore, an increase in the dilution rate leads to an increase in the Fe content in the coating, which weakens the effect of grain boundary strengthening and solid solution strengthening, thereby reducing the microhardness of the coating.

### Optimization and Characterization

Multitrack LC coatings are widely applied in product remanufacturing and surface modification. However, pore formation frequently occurs at the bottom of overlapping zones during laser cladding multitrack coatings (Ref 44). Previous works (Ref 45, 46) have stated that a large aspect ratio is vital to depositing porosity-free overlapped tracks. The aspect ratio of a single-track cladding layer can,

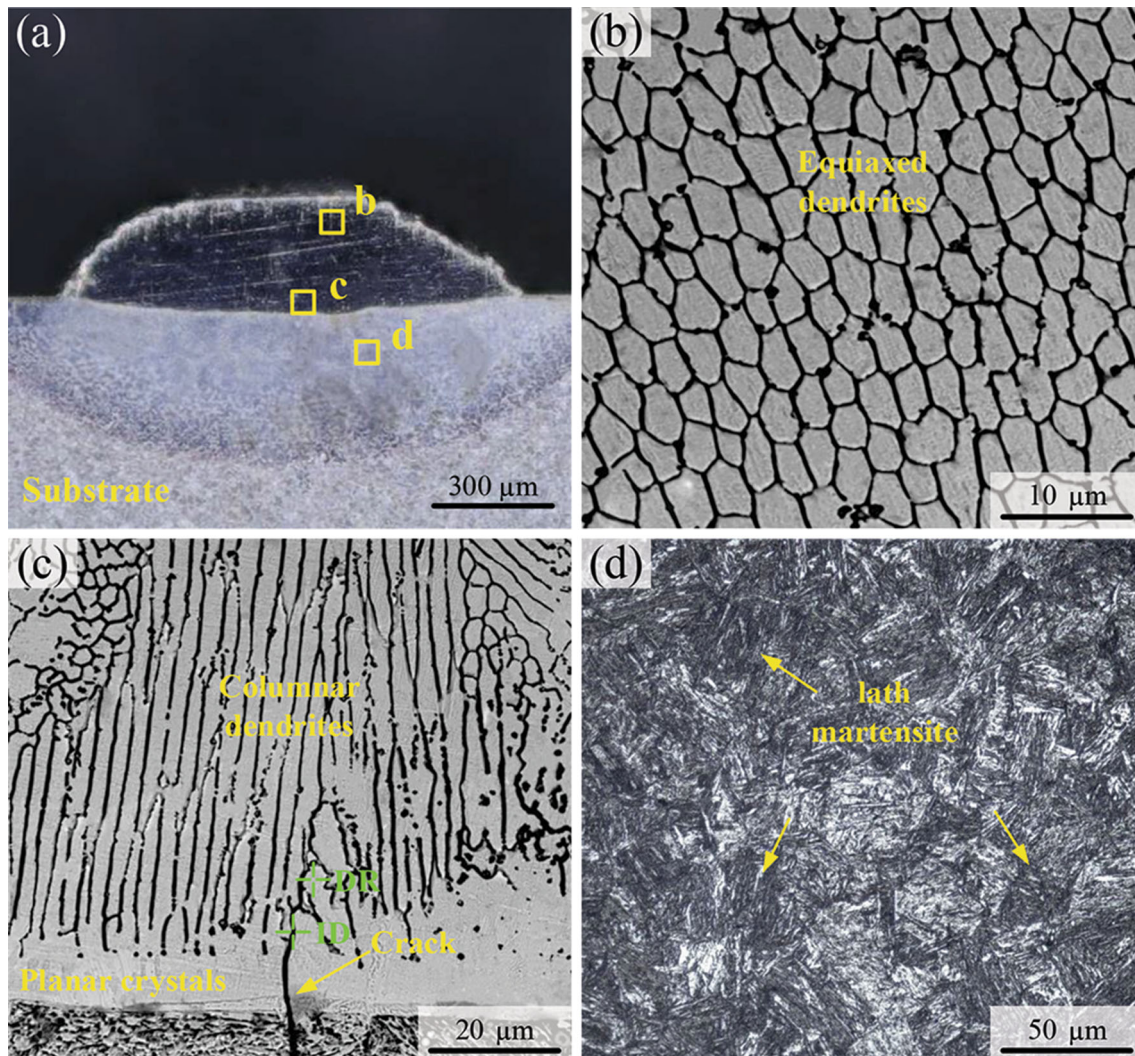
Table 6 Optimization criteria

Factors or response	Criterion	Limit		Importance
		Lower	Upper	
$P$ , W	In range	600	1100	3
$V$ , mm/s	In range	2	5	3
$F$ , g/min	In range	15	18	3
W/H	Maximize	1.67	5.88	3
$\eta$ , %	In range	10	20	3
Microhardness, HV	Maximize	155.13	184.72	3

therefore, be regarded as a quality criterion for laser cladding multitrack coatings. To better serve the industrial application of multitrack LC coatings, it is crucial to generate the largest aspect ratio to reduce porosity in the overlapping zones. The dilution rate is defined as the change degree of the coating composition caused by mixing of the melted substrate into the molten pool. A relatively low dilution rate cannot guarantee a good bonding quality between the coating and substrate. Conversely, a large dilution rate can change the element content in the coating, thereby affecting the coating’s performance. Generally, a dilution rate of 10~20% is recommended (Ref 47, 48). Therefore, this work aims to maximize the aspect ratio and microhardness and acquire a dilution rate of 10~20%. The corresponding optimization criteria for the process parameters and responses are listed in Table 6. The optimum process parameters given in Table 7 are laser power  $P = 773.65$  W, scanning speed  $V = 5$  mm/s and

**Table 7** Optimization and validation results

	$P$ , W	$V$ , mm/s	$F$ , g/min	W/H	$\eta$ , %	Microhardness, HV
Predicted	773.65	5.00	15.00	5.62	13.10	178.09
Actual	773.65	5.00	15.00	5.07	14.29	186.80
Error, %				9.8	9.1	4.9

**Fig. 10** Cross section of the optimized coating: (a) overall view; (b)–(d) magnified view of area b, c and d, respectively

powder feeding rate  $F = 15$  g/min. The cross-sectional morphology of the optimized CoCrCuFeNi coating is shown in Fig. 10(a). The validation results indicate that the errors between the predicted values and actual values for the aspect ratio, dilution rate and microhardness fall within 10%.

Figure 10(c) shows a magnified view of area c in Fig. 10(a). Planar crystals were observed in the transition zone between the coating and substrate, while columnar dendrites grow perpendicular to the substrate and appear above the transition zone. The grain morphology is mainly

determined by the cooling conditions during solidification, typically analyzed in terms of  $G/R$ , where  $G$  denotes the temperature gradient at the front of the solid–liquid interface, and  $R$  refers to the solidification rate (37). At the beginning of solidification, the temperature gradient  $G$  in front of the solid–liquid interface is very high, while  $R$  is low as the molten pool mainly releases heat to the substrate (Ref 49). A high  $G$  and low  $R$  provide favorable conditions for the growth of planar crystals in the transition zone. With the process of solidification, the solid–liquid interface moves upward, and the  $G/R$  value gradually decreases.

Columnar dendrites, roughly perpendicular to the substrate, are formed above the transition zone as the heat dissipates most rapidly along the direction perpendicular to the solid–liquid interface. The structure in the upper part of the coating is found to be equiaxed dendrites (Fig. 10b). Laser irradiation generates the highest temperature at the upper part of the molten pool, resulting in a low  $G$ .  $R$  here is much higher as the molten pool is in direct contact with the air. Regions with a relatively higher degree of undercooling and nucleation rate tend to form nondirectional equiaxed dendrites.

It is obvious in Fig. 10(c) that a longitudinal crack propagates throughout the transition zone. The EDS results for the dendrite and interdendrite areas shown in Fig. 10(c) are given in Table 8, where the dendrite and interdendrite are defined as DR and ID, respectively. Cu segregation is observed to occur in ID. As mentioned above, the solidification rate  $R$  in the cracking area is relatively low. Heard et al. (Ref 50) stated that for a rapid solidification alloy, the effective partition coefficient ( $k_{eff}$ ) of Cu is a function of  $R$ , that is, the degree of solute trapping (analyzed by  $k_{eff}$ ) decreases with decreasing  $R$ . Therefore, a lower  $R$  in the cracking area leads to a smaller  $k_{eff}$ , and, thus a weaker solute trapping effect of Cu (Ref 51), indicating a higher extent of Cu segregation in ID in the cracking area. Moreover, the lower melting point of Cu and its high mixing enthalpy with the other elements contribute to the weak bonding force between Cu and the other elements (Ref 52). Hence, Cu is easily excluded to ID by preferentially solidified metal (Ref 15), forming holes and pores in the subsequent solidification process. The existence of holes and pores impairs the coating’s ability to withstand internal stress, and it is prone to cracking in the presence of tensile stress/strain.

It is apparent from Fig. 10(d) that the microstructures in the heat-affected zone (HAZ) mainly consist of lath martensite. This can be ascribed to the fact that the temperature in HAZ exceeds the austenitizing temperature during LC and does not reach the melting point of the substrate. In the subsequent rapid cooling process, the microstructures in HAZ transform into martensite (Ref 31), which is called the martensitic transformation (MT). MT has a significant effect on the residual stress distribution

during LC. Wang et al. (Ref 53) and Du et al. (Ref 54) reported that the MT in HAZ increases the tensile stress in the coating, consequently generating cracks. The hardness improvement and the volume expansion of martensite in the HAZ during MT limits the substrate’s plastic deformation near the interface. The MT-induced tensile stress at the interface cannot be reduced via the substrate’s plastic deformation, which increases the cracking susceptibility of the coating. This might be another mechanism for crack propagation in the transition zone.

Figure 11 depicts the microhardness distribution in the cross section of the coating. The first microhardness test point was located near the coating surface, and 24 points were tested along the depth of the coating with an interval of 40  $\mu\text{m}$ . The microhardness near the coating surface was recorded to be 186.8 HV, which is obviously higher than that of the CoCrCuFeNi coating prepared by plasma transferred arc cladding (Ref 55). The hardness values are stable, indicating an evenly distributed structure inside the coating. The highest microhardness, close to 700 HV, was observed in HAZ. This can be ascribed to the vast existence of lath martensite (Fig. 10d), making the microhardness of the HAZ much higher than that of the 45 steel substrate.

The XRD test result presented in Fig. 12(a) shows that the phases in the CoCrCuFeNi coating possess a single FCC structure, similar to results obtained by previous studies (Ref 8, 15). Nonetheless, the XRD result alone does not confirm whether the coating belongs to the HEAs.

The mixing entropy is another essential criterion to confirm whether an alloy belongs to HEAs (Ref 56). The mixing entropy value of an alloy can be calculated from the Boltzmann equation (Eq. 10):

**Table 8** EDS results of areas in Fig. 10c (at.%)

Areas	Co	Cr	Cu	Fe	Ni
Nominal	20	20	20	20	20
DR	17.76	16.91	5.17	40.78	19.28
ID	14.41	13.49	16.68	38.81	16.62

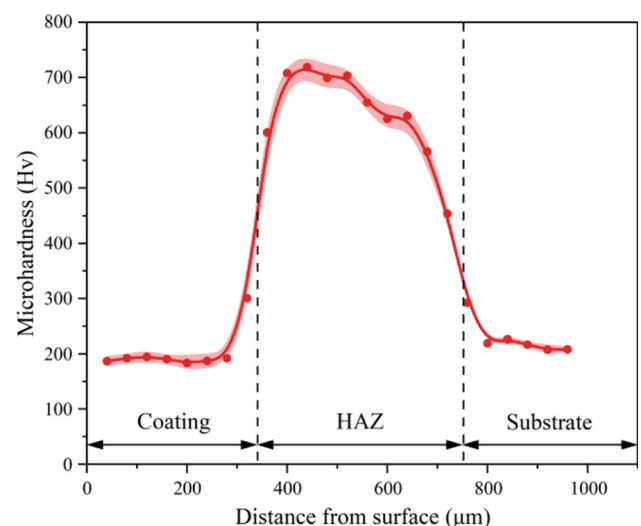


**Fig. 11** Microhardness distribution along the depth of the optimized coating.

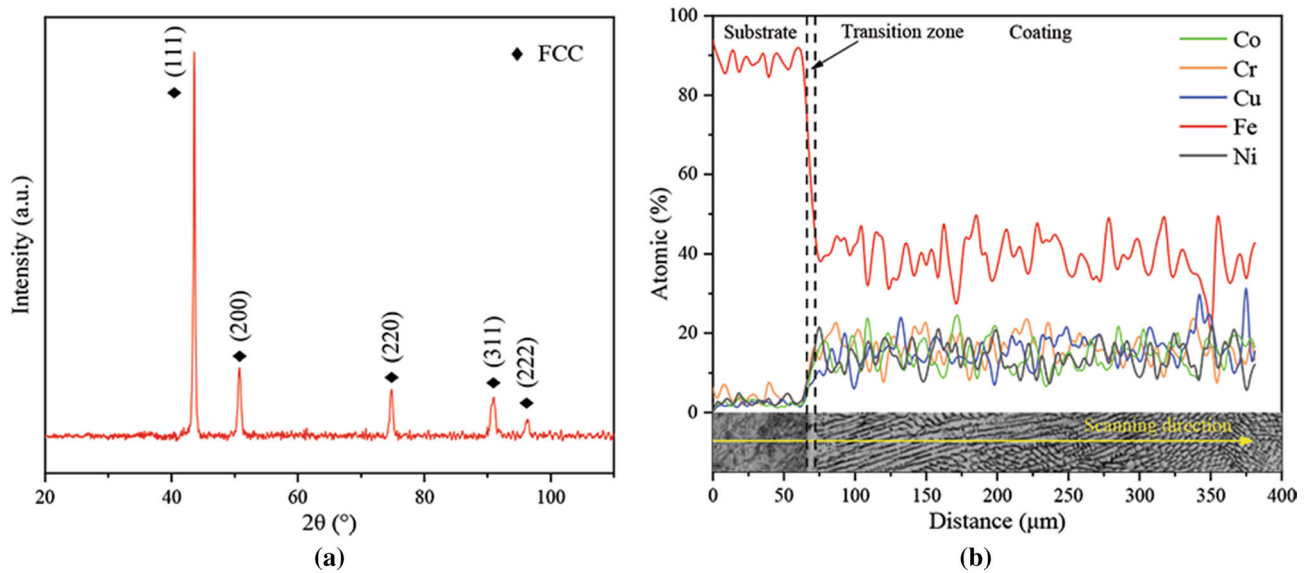


**Fig. 12** XRD and EDS results of the optimized coating: (a) XRD pattern and (b) EDS profile.

$$\Delta S_{mix} = -R \sum_{i=1}^n x_i \ln x_i \quad (\text{Eq 10})$$

where  $n$  is the number of elements,  $x_i$  refers to the atomic concentration of the  $i^{\text{th}}$  element and  $R$  represents the gas constant (8.314 J/K/mol).

Obviously, the theoretical mixing entropy of a five-element equimolar alloy is  $1.61R$ . However, Fe was mixed into the coating due to dilution. As a result, the content of each element in the CoCrCuFeNi coating deviates from the theoretical value, as shown in Fig. 12(b). Therefore, it is necessary to calculate the actual mixing entropy of the CoCrCuFeNi coating. The EDS results show that the atomic concentration of each element in the CoCrCuFeNi coating is Co 0.18, Cr 0.1477, Cu 0.1404, Fe 0.3664, and Ni 0.1655. The actual mixing entropy of the CoCrCuFeNi coating is thereby calculated to be  $1.53R > 1.5R$ , indicating that the coating belongs to HEAs (Ref 56). As shown in Fig. 12(b), the content of each element changes smoothly in the transition zone, revealing a good bonding quality between the coating and substrate. The thickness of the transition zone is approximately  $5 \mu\text{m}$ , which reveals a low dilution rate under optimum process parameters.

## Conclusions

Optimization of the process parameters for laser cladding CoCrCuFeNi HEA coatings on 45 steel was carried out via response surface methodology (RSM). The effect of process parameters on responses was systematically investigated, and statistical relationships between process

parameters and responses were established based on the regression models developed by RSM. The main results can be summarized as follows:

- 1) The aspect ratio increases with the laser power and scanning speed. When the laser power is kept low, a larger aspect ratio can be obtained with a higher or lower powder feeding rate. Reducing the laser power or increasing the scanning speed is beneficial for a low dilution rate. If the laser power remains constant, the dilution rate decreases at a higher or lower powder feeding rate. The microhardness increases with decreasing laser power and increasing scanning speed, while the powder feeding rate has little effect on the microhardness.
- 2) A laser power of 773.65 W, scanning speed of 5 mm/s and powder feeding rate of 15 g/min are found to be the optimum parameters. The aspect ratio, dilution rate and microhardness of the optimized CoCrCuFeNi coating are determined to be 5.07, 14.29% and 186.8 HV, respectively.
- 3) The microstructures inside the coating, from bottom to top, were found to consist of planar crystals, columnar dendrites and equiaxed dendrites. A longitudinal crack was observed to propagate throughout the transition zone, which can be attributed to the segregation of Cu in the interdendrite areas and the martensitic transformation in the heat-affected zone.
- 4) The phases in the coating possess a single FCC structure, and the mixing entropy of the coating is calculated to be  $1.53R$ , which together confirm that the optimized CoCrCuFeNi coating belongs to HEAs.

**Acknowledgments** The authors are grateful to the financial support from the National Natural Science Foundation of China (No. 51875050), the Hunan Provincial Key Research and Development Program (No. 2020GK2085, 2021GK2021), the Tribology Science Fund of State Key Laboratory of Tribology (SKLTKF21B08).

## References

- G.J. Zhang, Q.W. Tian, K.X. Yin, S.Q. Niu, M.H. Wu, W.W. Wang, Y.N. Wang and J.C. Huang, Effect of Fe on Microstructure and Properties of AlCoCrFeNi ( $x=1.5, 2.5$ ) High Entropy Alloy Coatings Prepared By Laser Cladding, *Intermetallics*, 2020, **119**, p 106722.
- Y. Tong, L. Bai, X. Liang, Y. Chen, Z. Zhang, J. Liu, Y. Li and Y. Hu, Influence of Alloying Elements on Mechanical and Electronic Properties of NbMoTaW ( $X = Cr, Zr, V, Hf$  and Re) Refractory High Entropy Alloys, *Intermetallics*, 2020, **126**, 106928.
- P. Niu, R. Li, S. Zhu, M. Wang, C. Chen and T. Yuan, Hot Cracking, Crystal Orientation and Compressive Strength of an Equimolar CoCrFeMnNi High-Entropy Alloy Printed by Selective Laser Melting, *Opt. Laser Technol.*, 2020, **127**, p106147.
- L. Bai, Y. Hu, X. Liang, Y. Tong, J. Liu, Z. Zhang, Y. Li and J. Zhang, Titanium Alloying Enhancement of Mechanical Properties of NbTaMoW Refractory High-Entropy Alloy: First-Principles and Experiments Perspective, *J. Alloys Compd.*, 2021, **857**, 157542.
- L. Jiang, W. Wu, Z. Cao, D. Deng and T. Li, Microstructure Evolution and Wear Behavior of the Laser Cladded CoFeNi<sub>2</sub>V<sub>0.5</sub>Nb<sub>0.75</sub> and CoFeNi<sub>2</sub>V<sub>0.5</sub>Nb High-Entropy Alloy Coatings, *J. Therm. Spray Technol.*, 2016, **25**(4), p 806–814.
- H. Liang, H. Yao, D. Qiao, S. Nie, Y. Lu, D. Deng, Z. Cao and T. Wang, Microstructures and Wear Resistance of AlCrFeNi<sub>2</sub>W<sub>0.2</sub>Nb<sub>x</sub> High-Entropy Alloy Coatings Prepared by Laser Cladding, *J. Therm. Spray Technol.*, 2019, **28**(6), p 1318–1329.
- V.K. Pandey, V. Shivam, B.N. Sarma and N.K. Mukhopadhyay, Phase Evolution and Thermal Stability of Mechanically Alloyed CoCrCuFeNi High Entropy Alloy, *Mater. Res. Express*, 2020, **6**(12), p 1265b9.
- H. Zhang, Y.-Z. He, Y. Pan and S. Guo, Thermally Stable Laser Cladded CoCrCuFeNi High-Entropy Alloy Coating With Low Stacking Fault Energy, *J. Alloys Compd.*, 2014, **600**, p 210–214.
- Y.Y. Liu, Z. Chen, Y.Z. Chen, J.C. Shi, Z.Y. Wang, S. Wang and F. Liu, Effect of Al Content on High Temperature Oxidation Resistance of Al<sub>x</sub>CoCrCuFeNi High Entropy Alloys ( $x=0, 0.5, 1, 1.5, 2$ ), *Vacuum*, 2019, **169**, p 108837.
- J. Dąbrowa, G. Cieślak, M. Stygar, K. Mroccka, K. Berent, T. Kulik and M. Danielewski, Influence of Cu Content on High Temperature Oxidation Behavior of AlCoCrCu<sub>x</sub>FeNi High Entropy Alloys ( $x = 0; 0.5; 1$ ), *Intermetallics*, 2017, **84**, p 52–61.
- X.W. Qiu, Y.P. Zhang and C.G. Liu, Effect of Ti Content on Structure and Properties of Al<sub>2</sub>CrFeNiCoCuTi<sub>x</sub> High-Entropy Alloy Coatings, *J. Alloys Compd.*, 2014, **585**, p 282–286.
- M. Löbel, T. Lindner, M. Grimm, L.-M. Rymer and T. Lampke, Influence of Aluminum and Molybdenum on the Microstructure and Corrosion Behavior of Thermally Sprayed High-Entropy Alloy Coatings, *J. Therm. Spray Technol.*, 2021 <https://doi.org/10.1007/s11666-021-01297-6>
- Z.U. Arif, M.Y. Khalid, E. urRehman, S. Ullah, M. Atif and A. Tariq, A review on Laser Cladding of High-Entropy Alloys, Their Recent Trends and Potential Applications, *J. Manuf. Process*, 2021, **68**, p 225–273.
- K. Huang, L. Chen, X. Lin, H. Huang, S. Tang and F. Du, Wear and Corrosion Resistance of Al<sub>0.5</sub>CoCrCuFeNi High-Entropy Alloy Coating Deposited on AZ91D Magnesium Alloy by Laser Cladding, *Entropy*, 2018, **20**(12), p 915.
- Y. Li and Y. Shi, Microhardness, Wear Resistance, and Corrosion Resistance of Al<sub>x</sub>CrFeCoNiCu High-Entropy Alloy Coatings on Aluminum By Laser Cladding, *Opt. Laser Technol.*, 2021, **134**, p106632.
- Y. Cui, J. Shen, S.M. Manladan, K. Geng and S. Hu, Wear Resistance of FeCoCrNiMnAl<sub>x</sub> High-Entropy Alloy Coatings at High Temperature, *Appl. Surf. Sci.*, 2020, **512**, 145736.
- G. Jin, Z. Cai, Y. Guan, X. Cui, Z. Liu, Y. Li, M. Dong and D. Zhang, High Temperature Wear Performance of Laser-Cladded FeNiCoAlCu High-Entropy Alloy Coating, *Appl. Surf. Sci.*, 2018, **445**, p 113–122.
- M. Erfanmanesh, H. Abdollah-Pour, H. Mohammadian-Semnani and R. Shoja-Razavi, An Empirical-Statistical Model for Laser Cladding of WC-12Co Powder on AISI 321 Austenitic Steel, *Opt. Laser Technol.*, 2017, **97**, p 180–186.
- Q. Chao, T. Guo, T. Jarvis, X. Wu, P. Hodgson and D. Fabijanic, Direct Laser Deposition Cladding of Al<sub>3</sub>CoCrFeNi High Entropy Alloys on a High-Temperature Stainless Steel, *Surf. Coat. Technol.*, 2017, **332**, p 440–451.
- F. Shu, B. Zhang, T. Liu, S. Sui, Y. Liu, P. He, B. Liu and B. Xu, Effects of Laser Power on Microstructure and Properties of Laser Cladded CoCrBFeNiSi High-Entropy Alloy Amorphous Coatings, *Surf. Coat. Technol.*, 2019, **358**, p 667–675.
- Y. Zhang, T.-F. Han, M. Xiao and Y.-F. Shen, Effect of Process Parameters on the Microstructure and Properties of Laser-Clad FeNiCoCrTi<sub>0.5</sub> High-Entropy Alloy Coating, *Int. J. Miner. Metall. Mater.*, 2020, **27**(5), p 630–639.
- C. Ni, Y. Shi, J. Liu and G. Huang, Characterization of Al<sub>0.5</sub>FeCu<sub>0.7</sub>NiCoCr High-Entropy Alloy Coating on Aluminum Alloy by Laser Cladding, *Opt. Laser Technol.*, 2018, **105**, p 257–263.
- T.M. Yue, H. Xie, X. Lin, H.O. Yang and G.H. Meng, Solidification Behaviour in Laser Cladding of AlCoCrCuFeNi High-Entropy Alloy on Magnesium Substrates, *J. Alloys Compd.*, 2014, **587**, p 588–593.
- S. Liu and R. Kovacevic, Statistical Analysis and Optimization of Processing Parameters in High-Power Direct Diode Laser Cladding, *Int. J. Adv. Manuf. Technol.*, 2014, **74**(5–8), p 867–878.
- M. Ma, W. Xiong, Y. Lian, D. Han, C. Zhao and J. Zhang, Modeling and Optimization for Laser Cladding Via Multi-Objective Quantum-Behaved Particle Swarm Optimization Algorithm, *Surf. Coat. Technol.*, 2020, **381**, p125129.
- M. Dada, P. Popoola, N. Mathe, S. Pityana and S. Adeosun, Parametric Optimization of Laser Deposited High Entropy Alloys Using Response Surface Methodology (RSM), *Int. J. Adv. Manuf. Technol.*, 2020, **109**(9–12), p 2719–2732.
- A.A. Siddiqui, A.K. Dubey and C.P. Paul, Geometrical Characteristics in Laser Surface Alloying of a High-entropy Alloy, *Lasers Eng.*, 2019, **43**, p 237–259.
- Y. Cai, Y. Chen, S.M. Manladan, Z. Luo, F. Gao and L. Li, Influence of Dilution Rate on the Microstructure and Properties of FeCrCoNi High-Entropy Alloy Coating, *Mater. Des.*, 2018, **142**, p 124–137.
- H. Wang, W. Zhang, Y. Peng, M. Zhang, S. Liu and Y. Liu, Microstructures and Wear Resistance of FeCoCrNi-Mo High Entropy Alloy/Diamond Composite Coatings by High Speed Laser Cladding, *Coatings*, 2020, **10**(3), p 300.
- Verma, P. Tarate, A.C. Abhyankar, M.R. Mohape, D.S. Gowtam, V.P. Deshmukh and T. Shanmugasundaram, High Temperature Wear in CoCrFeNiCu<sub>x</sub> High Entropy Alloys: The role of Cu, *Scr. Mater.*, 2019, **161**, p 28–31.
- Z. Wu, T. Li, Q. Li, B. Shi, X. Li, X. Wang, H. Lu and H.-C. Zhang, Process Optimization of Laser Cladding Ni60A Alloy

- Coating in Remanufacturing, *Opt. Laser Technol.*, 2019, **120**, 105718.
32. H. Mirhosseini, C.P. Tan, A.R. Taherian and H.C. Boo, Modeling the Physicochemical Properties of Orange Beverage Emulsion as Function of Main Emulsion Components Using Response Surface Methodology, *Carbohydr. Polym.*, 2009, **75**(3), p 512–520.
  33. S.T. Nyadongo, E.O. Olakanmi and S.L. Pityana, Experimental and Numerical Analyses of Geometrical and Microstructural Features of Tribaloy T-800 Composite Coating Deposited Via Laser Cladding-Assisted With Pre-Heat (LCAP) Process, *J. Manuf. Process.*, 2021, **69**, p 84–111.
  34. S. Mohammed, Z. Zhang and R. Kovacevic, Optimization of Processing Parameters in Fiber Laser Cladding, *Int. J. Adv. Manuf. Technol.*, 2020, **111**(9–10), p 2553–2568.
  35. R. Saeedi, R.S. Razavi, S.R. Bakhshi, M. Erfanmanesh and A.A. Bani, Optimization and Characterization of Laser Cladding of NiCr and NiCr–TiC Composite Coatings on AISI 420 Stainless Steel, *Ceram. Int.*, 2021, **47**(3), p 4097–4110. <https://doi.org/10.1016/j.ceramint.2020.09.284>
  36. Y. Li, K. Su, P. Bai and L. Wu, Microstructure and Property Characterization of Ti/TiBCN Reinforced Ti Based Composite Coatings Fabricated By Laser Cladding With Different Scanning Speed, *Mater. Charact.*, 2020, **159**, 110023.
  37. P. Fan and G. Zhang, Study on Process Optimization of WC-Co50 Cermet Composite Coating by Laser Cladding, *Int. J. Refract. Metals Hard Mater.*, 2020, **87**, 105133.
  38. B. Ondicho and N. Alunda, Park, Effect of Fe on the Hall-Petch Relationship of  $(\text{CoCrMnNi})_{100-x}\text{Fe}_x$  Medium-and High-Entropy Alloys, *Intermetallics*, 2021, **136**, p 107239.
  39. E.-O. Hall, The Deformation and Ageing of Mild Steel: III Discussion of Results, *Proc. Phys. Soc. B*, 1951, **64**(9), p 747–753.
  40. N.J. Petch, The Cleavage Strength of Polycrystals, *J. Iron Steel Inst.*, 1953, **174**(19), p 25–28.
  41. Q. Chen, K. Zhou, L. Jiang, Y. Lu and T. Li, Effects of Fe Content on Microstructures and Properties of AlCoCrFe<sub>x</sub>Ni High-Entropy Alloys, *Arab. J. Sci. Eng.*, 2015, **40**(12), p 3657–3663.
  42. M.P. Agustianingrum, I. Ondicho, D.E. Jodi, N. Park and U. Lee, Theoretical Evaluation of Solid Solution Interaction in Fe<sub>x</sub>(-CoCrMnNi)<sub>100-x</sub> Medium-and High-Entropy Alloys, *Mater. Sci. Eng. A*, 2019, **759**, p 633–639.
  43. Z. Wang, Q. Wu, W. Zhou, F. He, C. Yu, D. Lin, J. Wang and C.T. Liu, Quantitative Determination of The Lattice Constant in High Entropy Alloys, *Scr. Mater.*, 2019, **162**, p 468–471.
  44. C. Zhou, S. Zhao, Y. Wang, Fa. Liu, W. Gao, X. Lin, Mitigation of Pores Generation At Overlapping Zone During Laser Cladding, *J. Mater. Process. Technol.*, 2015, **216**, p 369–374.
  45. A.J. Pinkerton, W. Wang and L. Li, Component Repair Using Laser Direct Metal Deposition, *Proc. Inst. Mech. Eng. B J. Eng. Manuf.*, 2008, **222**, p 823–836.
  46. T.E. Abioye, J. Folkes and A.T. Clare, A Parametric Study of Inconel 625 Wire Laser Deposition, *J. Mater. Process. Technol.*, 2013, **213**, p 2145–2151.
  47. P. Alvarez, M. Montealegre, J. Pulido-Jiménez and J. Arrizubieta, Analysis of the Process Parameter Influence in Laser Cladding of 316L Stainless Steel, *JMMP*, 2018, **2**(3), p 55.
  48. E.W.A. Figueredo, L.H.R. Apolinario, M.V. Santos, A.C.S. Silva, J.A. Avila, M.S.F. Lima and T.F.A. Santos, Influence of Laser Beam Power and Scanning Speed on the Macrostructural Characteristics of AISI 316L and AISI 431 Stainless Steel Depositions Produced by Laser Cladding Process, *J. Materi. Eng. Perform.*, 2021, **30**(5), p 3298–3312.
  49. C. Wang, S. Zhang, C.H. Zhang, C.L. Wu, J.B. Zhang and A.O. Abdullah, Phase Evolution and Wear Resistance of in Situ Synthesized V<sub>8</sub>C<sub>7</sub> Particles Reinforced Fe-Based Coating By Laser Cladding, *Opt. Laser Technol.*, 2018, **105**, p 58–65.
  50. D.W. Heard, J. Boselli, R. Rioja, E.A. Marquis, R. Gauvin and M. Brochu, Interfacial Morphology Development and Solute Trapping Behavior During Rapid Solidification of An Al–Li–Cu Alloy, *Acta Mater.*, 2013, **61**(5), p 1571–1580.
  51. P.M. Smith and M.J. Aziz, Solute Trapping in Aluminum-Alloys, *Acta Metall. Mater.*, 1994, **42**, p 3515–3525.
  52. Q.C. Fan, B.S. Li and Y. Zhang, Influence of Al and Cu Elements on the Microstructure and Properties of (FeCrNiCo)Al<sub>x</sub>Cu<sub>y</sub> High-Entropy Alloys, *J. Alloys Compd.*, 2014, **614**, p 203–210.
  53. D. Wang, Q. Hu and X. Zeng, Residual Stress and Cracking Behaviors of Cr<sub>13</sub>Ni<sub>5</sub>Si<sub>2</sub> Based Composite Coatings Prepared By Laser-Induction Hybrid Cladding, *Surf. Coat. Technol.*, 2015, **274**, p 51–59.
  54. C. Du, L. Hu, X. Ren, Y. Li, F. Zhang, P. Liu and Y. Li, Cracking Mechanism of Brittle FeCoNiCrAl HEA Coating Using Extreme High-Speed Laser Cladding, *Surf. Coat. Technol.*, 2021, **424**, p127617.
  55. J.B. Cheng, X.B. Liang and B.S. Xu, Effect of Nb Addition on the Structure and Mechanical Behaviors of CoCrCuFeNi High-Entropy Alloy Coatings, *Surf. Coat. Technol.*, 2014, **614**, p 203–210.
  56. J.-W. Yeh, Alloy Design Strategies and Future Trends in High-Entropy Alloys, *JOM*, 2013, **65**(12), p 1759–1771.

**Publisher's Note** Springer Nature remains neutral with regard to jurisdictional claims in published maps and institutional affiliations.